Four-band tight-binding model of TiSiCO-family monolayers

Chaoxi Cui, Yilin Han, Ting-Ting Zhang, Zhi-Ming Yu, and Yugui Yao

Phys. Rev. B **108**, 155115 — Published 10 October 2023

DOI: 10.1103/PhysRevB.108.155115

Four-band tight-binding model of TiSiCO-family monolayers

Chaoxi Cui,[1, 2] Yilin Han,[1, 2] Ting-Ting Zhang,[3] Zhi-Ming Yu,[1, 2, *] and Yugui Yao[1, 2]

[1] *Centre for Quantum Physics, Key Laboratory of Advanced Optoelectronic Quantum Architecture and Measurement (MOE), School of Physics, Beijing Institute of Technology, Beijing 100081, China*

[2] *Beijing Key Lab of Nanophotonics & Ultrafine Optoelectronic Systems, School of Physics, Beijing Institute of Technology, Beijing 100081, China*

[3] *Beijing National Laboratory for Condensed Matter Physics, Institute of Physics, Chinese Academy of Sciences, Beijing 100190, China*

The TiSiCO-family monolayers have recently been attracting significant attention due to their unique valley-layer coupling (VLC). In this work, we present a minimal, four-band tight-binding (TB) model to capture the low-energy physics of the TiSiCO-family monolayers $Z_2Y\mathrm{CO}_2$ (Z = Ti, Zr, Hf; Y = Si, Ge) with strong VLC. These monolayers comprise two Z atom layers separated by approximately 4 Å in the out-of-plane direction. Around each valley (X or X'), the conduction and valence bands are mainly dominated by the $A_1\{d_{z^2(x^2-y^2)}\}$ and $B_2\{d_{yz}\}$ orbitals of the top Z atoms,and the $A_1\{d_{z^2(x^2-y^2)}\}$ and $B_1\{d_{xz}\}$ orbitals of the bottom Z atoms. Using these four states as a basis, we construct a symmetry-allowed TB model. Through parameter fitting from first-principles calculations, the four-band TB model not only reproduces the electronic band structure, but also captures the strong VLC, high-order topology, and valley-contrasting linear dichroism of the monolayers. Furthermore, the TB model reveals that these monolayers may exhibit various intriguing topological phases under electric fields and biaxial strains. Hence, the TB model established here can serve as the starting point for future research exploring the physics related to VLC and the $Z_2Y\mathrm{CO}_2$ monolayers.

I. INTRODUCTION

Valleytronics materials, which are characterized by the presence of multiple symmetry-connected energy extremal points in the low-energy bands, have been a focus of research in condensed matter physics [1–8]. The concept of valleytronics works in both three dimensions and two dimensions. However, due to the flexibility and controllability in two dimensions, it is the discovery of two-dimensional (2D) valleytronics materials like graphene and transitional metal dichalcogenides (TMDs) that leads to the rapid growth in the field of valleytronics [9, 10]. The 2D valleytronics materials are particularly attractive for both fundamental studies and the development of application devices [11–32].

Recently, the TiSiCO-family monolayers $Z_2Y\mathrm{CO}_2$ (Z =Ti, Zr, Hf; Y=Si, Ge) have been proposed as a novel class of 2D valleytronics materials [33]. Similar to the graphene and TMDs, both the conduction and valence bands of these monolayers exhibit two valleys located at two high-symmetry points of the Brillouin zone (BZ), namely, X and X' (Y) points. However, the two valleys in monolayer $Z_2Y\mathrm{CO}_2$ are time-reversal $\mathcal{T}$ invariant points and are connected by the spatial operators S_{4z} and $C_{2,110}$, which is completely different from that in the graphene and TMDs [5, 34–38]. As a result, the valley polarization in monolayer $Z_2Y\mathrm{CO}_2$ can be realized by the methods that do not break $\mathcal{T}$ symmetry. Particularly, due to the strong VLC–the conduction or valence electrons in different valleys have strong but opposite layer polarization, the gate electric field is an intuitive and efficient way to generate valley polarization in monolayer $Z_2Y\mathrm{CO}_2$. This electric control of valley polarization is highly desirable for the applications. In addition to static control, dynamical generation of valley polarization also can be realized in these monolayers, as they exhibit valley-contrasting linear dichroism [33]. Furthermore, it has been predicted that the monolayer $Z_2Y\mathrm{CO}_2$ is not a normal semiconductor but a second-order topological insulator [39]. Therefore, monolayer $Z_2Y\mathrm{CO}_2$ will be of broad interest to multiple fields, including valleytronics, 2D materials, optoelectronics, and higher-order topology.

In our previous work, an effective two-band $\boldsymbol{k\cdot p}$ model was developed based on invariant theory [33], where the spin-orbit coupling (SOC) effect is not included due to negligible SOC in the low-energy bands of the monolayer $Z_2Y\mathrm{CO}_2$. The effective model clearly demonstrates the coupling between valley and layer degrees of freedom, and can be used to describe the optical properties of the monolayer $Z_2Y\mathrm{CO}_2$. However, it is insufficient to capture the higher-order topology of systems and the physics away from the two valleys.

In this work, we present a minimal lattice model for the monolayer $Z_2Y\mathrm{CO}_2$ without SOC effect. The TB model is constructed by the d orbitals of Z atoms, i.e. the $A_1\{d_{z^2(x^2-y^2)}\}$ and $B_2\{d_{yz}\}$ orbitals of the top Z atoms, and the $A_1\{d_{z^2(x^2-y^2)}\}$ and $B_1\{d_{xz}\}$ orbitals of the bottom Z atoms. This effective model contains four bands: two valence bands and two conduction bands. All parameters in the model are obtained by fitting the electronic bands from the first-principles calculations. We demonstrate that our four-band TB model can effectively describe the low-energy physics of the monolayer $Z_2Y\mathrm{CO}_2$, including strong VLC, optical properties, and

* zhiming_yu@bit.edu.cn

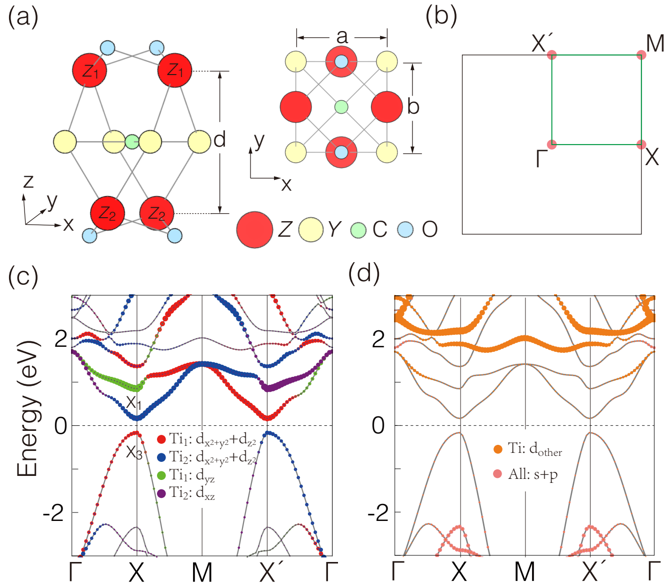

FIG. 1. (a) Side and top views of monolayer $Z_2Y\mathrm{CO}_2$. $a = b$ is the lattice constant and d refers to the vertical distance between the two Z atoms. (b) denotes the BZ of the monolayer. (c-d) show a representative example of orbital-projected band structures for the monolayer $Z_2Y\mathrm{CO}_2$ calculated from first-principle calculations. Here, Z and Y represent Ti and Si, respectively. (c) presents the orbitals included in the TB model, while (d) displays the other orbitals that are not incorporated in the model.

higher-order topology. Furthermore, the TB model suggests that the monolayer $Z_2Y\mathrm{CO}_2$ may undergo multiple phase transitions under external fields.

This paper is organized as follows. In Sec. II, we introduce the processes that lead to our four-band lattice model. In Sec. III, the optical and topological properties of the effective lattice model are studied. We investigate possible phase transitions of the model under external field in Sec. IV. Conclusions are given in Sec. V.

II. THE MINIMAL LATTICE MODEL

The monolayer $Z_2Y\mathrm{CO}_2$ belongs to layer group (LG) NO. 59 or space group (SG) No. 115 with D_{2d} point-group symmetry. All the monolayers share similar crystalline structures which is shown in Fig. 1(a), and their lattice constant ($a = b$) and height d are shown in Tab. I. One can find that the Z, Y, C, and O atoms are located at $2g$, $1b$, $1a$ and $2g$ Wyckoff positions, respectively. Figure 1(b) shows the Brillouin zone (BZ) of the monolayers with the high-symmetry points being labeled. Here, the position of the X point is $(\pi, 0)$ and that of X' point is $(0, \pi)$. Notice that there exists an alternative notation [40] where the positions of X and X' points are interchanged, which is adopted in our previous work [33]. In Fig. 1(c-d), we plot the electronic band of the monolayer $\mathrm{Ti_2SiCO_2}$. The electronic band of the other monolayers

TABLE I. The lattice constant ($a = b$) and height (d) of the monolayer $Z_2Y\mathrm{CO}_2$ (Z =Ti, Zr, Hf; Y=Si, Ge).

Material	$a=b$	d	Material	$a=b$	d
$\mathrm{Ti_2SiCO_2}$	2.82 Å	4.10 Å	$\mathrm{Ti_2GeCO_2}$	2.89 Å	4.16 Å
$\mathrm{Zr_2SiCO_2}$	3.01 Å	4.26 Å	$\mathrm{Zr_2GeCO_2}$	3.06 Å	4.29 Å
$\mathrm{Hf_2SiCO_2}$	2.98 Å	4.18 Å	$\mathrm{Hf_2GeCO_2}$	3.04 Å	4.21 Å

can be found in Fig. 6.

Around Fermi level, the electronic bands of these monolayers mainly consist of certain d orbitals of the two Z atoms, while the contribution of other orbits, i.e., other d orbit of Z atoms, and s and p orbit of all other atoms is negligible, as shown in Fig. 1(c-d) and appendix (Fig. 6). Specifically, the low-energy bands at X (X') valley are dominated by the d_{yz} (d_{xz}) orbitals of the top (bottom) Z atoms, and the d_{z^2} and $d_{x^2-y^2}$ orbitals of the both top and bottom Z atoms [see Fig. 1(c)]. From these band analysis, one knows that the valley states including both conduction and valence valley states have strong layer polarization, and the layers polarization for the X and X' valleys are opposite, leading to strong VLC effect. The VLC effect is protected by the S_{4z} and $C_{2,110}$ symmetries. The band representation of the conduction (valence) band edge at X valley is calculated as X_1 (X_3) [41], from which the band representation of the band edges at X' valley can be inferred.

The site symmetry group of the Z atoms (Wyckoff position $2g$ in SG No. 115) is C_{2v}. For spinless systems, the d orbitals in C_{2v} point-group symmetry would split into five non-degenerate energy levels: $2A_1 + A_2 + B_1 + B_2$, as listed in Table II. Since the d_{z^2} and $d_{x^2-y^2}$ orbitals share the same representation A_1 of the C_{2v} point group, it is unnecessary to distinguish them in the band analysis. Therefore, for simplification, we only use the d_{z^2} and d_{yz} orbitals of the top Z atom and the d_{z^2} and d_{xz} orbitals of the bottom Z atom to construct a four-band model. It can be proved that the four-band model is the minimal one to capture the physics of the monolayer $Z_2Y\mathrm{CO}_2$. First, since there are two Z atoms in a unit cell, the band

TABLE II. The first two columns show the compatibility relaxation between d-orbitals and the irreducible representations (IRRs) of C_{2v} point group. The last column presents the band representation (BR) of SG 115 from $2g$ Wyckoff position, for which the site symmetry is C_{2v}.

d-orbital	IRRs	Induced BRs ($R \uparrow G$)			
		$R \uparrow G$	Γ	X	M
d_{z^2}, $d_{x^2-y^2}$	A_1	$A_1 \uparrow G$	$\Gamma_1 \oplus \Gamma_2$	$X_1 \oplus X_3$	M_5
d_{xy}	A_2	$A_2 \uparrow G$	$\Gamma_3 \oplus \Gamma_4$	$X_2 \oplus X_4$	M_5
d_{xz}	B_1	$B_1 \uparrow G$	Γ_5	$X_2 \oplus X_3$	$M_3 \oplus M_4$
d_{yz}	B_2	$A_2 \uparrow G$	Γ_5	$X_1 \oplus X_4$	$M_1 \oplus M_2$

TABLE III. Fitted parameters of the four-band TB model for monolayer $Z_2Y\mathrm{CO}_2$ with inter-layer and intra-layer NN hoppings based on first-principle calculations. "t" and "r" stand for inter-layer NN and intra-layer NN hoppings, respectively. All parameters are in unit of eV.

	Δ	$t_{1,x}$	$t_{1,y}$	$t_{2,x}$	$t_{2,y}$	t'	r_1	r_2	r'
TiSiCO	0.036	-1.457	-1.731	1.242	2.225	1.354	-1.421	-1.289	-0.508
TiGeCO	0.137	-1.766	-2.115	1.561	2.647	1.535	-1.697	-1.201	-0.882
ZrSiCO	0.063	-1.853	-2.491	1.397	3.185	2.094	-2.007	-1.673	-1.292
ZrGeCO	0.06	-2.014	-2.557	1.404	3.069	1.963	-2.107	-1.458	-1.22
HfSiCO	0.021	-2.124	-2.879	1.599	3.782	2.332	-2.574	-2.039	-1.524
HfGeCO	0.042	-2.289	-2.892	1.395	3.174	2.164	-2.729	-1.633	-1.328

number of the lattice model must be even. Second, the band representations of the SG No. 115 (with $\mathcal{T}$ symmetry) from $2g$ Wyckoff position can be found in the BCS website [40, 42], and are rewritten in Table II. From Table II, one observes that a two-band lattice model based on the d orbitals of Z atom must be a semimetal, as the two bands will be degenerate at Γ or M points. However, the monolayer $Z_2Y\mathrm{CO}_2$ is a semiconductor rather than a semimetal. This contradiction indicates that the lattice model of the monolayer $Z_2Y\mathrm{CO}_2$ should have (at least) four bands.

To construct the lattice model, we need to determine the matrix representations of the generators of the SG 115. The basis of the TB model here is $\{d^1_{z^2}, d^1_{yz}, d^2_{z^2}, d^2_{xz}\}$, where the superscript 1(2) denotes the top (bottom) Z atom, located at $(0, b/2, d/2)$ and $(a/2, 0, -d/2)$, respectively. The generators of the symmetry operators of the monolayer $Z_2Y\mathrm{CO}_2$ are S_{4z}, M_y and $\mathcal{T}$, and their matrix representations are obtained as:

$$S_{4z} = \begin{bmatrix} 0 & 0 & -1 & 0 \\ 0 & 0 & 0 & 1 \\ -1 & 0 & 0 & 0 \\ 0 & -1 & 0 & 0 \end{bmatrix}, \; M_y = \begin{bmatrix} 1 & 0 & 0 & 0 \\ 0 & -1 & 0 & 0 \\ 0 & 0 & 1 & 0 \\ 0 & 0 & 0 & 1 \end{bmatrix}, \quad (1)$$

and

$$\mathcal{T} = \begin{bmatrix} 1 & 0 & 0 & 0 \\ 0 & 1 & 0 & 0 \\ 0 & 0 & 1 & 0 \\ 0 & 0 & 0 & 1 \end{bmatrix} \mathcal{K}, \quad (2)$$

where $\mathcal{K}$ is complex conjugation operator. Then, the symmetry-allowed TB Hamiltonian of the monolayer $Z_2Y\mathrm{CO}_2$ is established as

$$\mathcal{H} = \begin{pmatrix} H_{\mathrm{top}} & H_{\mathrm{inter}} \\ H^{\dagger}_{\mathrm{inter}} & H_{\mathrm{bottom}} \end{pmatrix}, \quad (3)$$

with $H_{\mathrm{bottom}}(k_x, k_y) = H_{\mathrm{top}}(k_y, -k_x)$,

$$H_{\mathrm{top}} = \Delta\sigma_3 + \begin{pmatrix} \sum_{\alpha=x,y} t_{1,\alpha}\cos k_\alpha & it'\sin k_y \\ -it'\sin k_y & \sum_{\alpha=x,y} t_{2,\alpha}\cos k_\alpha \end{pmatrix},$$

and

$$H_{\mathrm{inter}} = \begin{pmatrix} r_1 \cos\frac{k_x}{2}\cos\frac{k_y}{2} & ir'\cos\frac{k_x}{2}\sin\frac{k_y}{2} \\ ir'\cos\frac{k_y}{2}\sin\frac{k_x}{2} & r_2\sin\frac{k_x}{2}\sin\frac{k_y}{2} \end{pmatrix}.$$

Here, σ_3 is the third component of the Pauli matrix, and all the parameters are real. The Hamiltonian (3) contains the nearest-neighbor (NN) intra-layer and NN inter-layer hoppings (see Appendix B), resulting in 9 symmetry-allowed real parameters. We employ the gradient descent method [43] to determine the parameters by comparing the electronic bands from the first-principles calculations with those from the TB model (3) with appropriate initial parameters. The fitted bands of the monolayer $Z_2Y\mathrm{CO}_2$ are illustrated in Fig. 2 and the corresponding parameters are listed in Table III. Although this TB model captures the essential and low-energy physics of the monolayer $Z_2Y\mathrm{CO}_2$, it fails to describe the physics of the material at high-energy, such as that at Γ and M points. Generally, one can improve the fitting by adding more hoppings or more orbits [36].

As studied in Ref. [33], one of the most intriguing properties of the monolayer $Z_2Y\mathrm{CO}_2$ is the strong VLC effect. To demonstrate that our TB model can capture the VLC effect, we present the layer polarization of the valley states of the TB model in Fig. 3. The layer polarization is defined as [33]

$$P_n(\boldsymbol{k}) = \int_{z>0} |\psi_{n\boldsymbol{k}}|^2 \, d\boldsymbol{r} - \int_{z<0} |\psi_{n\boldsymbol{k}}|^2 \, d\boldsymbol{r}, \quad (4)$$

with $\psi_{n\boldsymbol{k}}$ representing the eigenstate of n-th Bloch band, i.e. the eigenstate of the TB Hamiltonian (3), and $\boldsymbol{k}$ denoting the wave vector. Here, the $z = 0$ plane is set on the middle Y/C atom layer. The layer polarization $P_n(\boldsymbol{k})$ indicates the polarization of $\psi_{n\boldsymbol{k}}$ between the top $(z > 0)$ and bottom $(z < 0)$ layers. From Fig. 3, strong valley-contrasted layer polarization can be observed for both

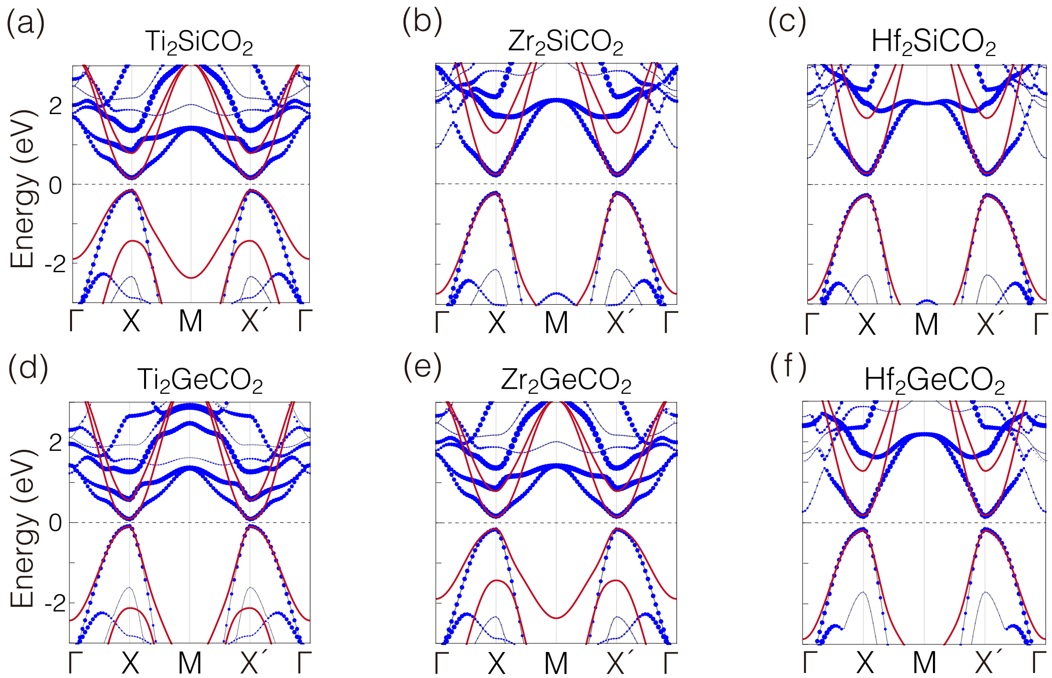

FIG. 2. (a-f) The TB band structures (red) for monolayer $Z_2Y\mathrm{CO}_2$ are compared with the first-principles band structures (gray). The blue dots indicate the band components of orbitals included in the TB model.

conduction and valence bands, reproducing the VLC effect in the monolayer $Z_2Y\mathrm{CO}_2$.

III. OPTICAL AND TOPOLOGICAL PROPERTIES

In this section, we show that the four-band TB model can describe the optical and topological properties of the monolayer $Z_2Y\mathrm{CO}_2$. TMDs are known to exhibit valley-contrasting circular dichroism in optical interband absorption [5, 37, 44]. However, due to the difference in symmetry, the X (X') valleys in monolayer $Z_2Y\mathrm{CO}_2$ exclusively couple to x-linearly (y-linearly) polarized light [33] rather than the circularly polarized light. Consequently, the monolayer $Z_2Y\mathrm{CO}_2$ features valley-contrasting linear dichroism. The $\boldsymbol{k}$-resolved linear polarization degree of the optical interband absorption between valence and conduction bands is characterized by

$$\eta(\boldsymbol{k}) = \frac{|M_x|^2-|M_y|^2}{|M_x|^2+|M_y|^2} \tag{5}$$

where $M_i = \langle\psi_{\mathrm{ck}}|\frac{\partial H}{\partial k_i}|\psi_{\mathrm{vk}}\rangle$ is the coupling strength between valence and conduction band with the optical field linearly polarized in the i-th direction. $\eta(\boldsymbol{k})$ indicates the normalized absorption difference between x and y-linearly polarized light. The $\eta(\boldsymbol{k})$ calculated from our TB model is shown in Fig. 4(a). We find that $\eta(X) = 1$ and $\eta(X') = -1$, indicating an opposite linear dichroism around the X and X' valleys. This is consistent with the results in Ref. [33]. Moreover, since the four high-symmetry lines, Γ-X, Γ-X', M-X, and M-X' have mirror symmetry (M_x or M_y), the electronic states on them must exclusively couple to a linearly polarized light whose polarization direction is either parallel or perpendicular to the mirror. This property also can be found in our calculations, where $\eta(\boldsymbol{k}) = \pm 1$ for the four high-symmetry lines [see Fig. 4(a)].

Our four-band TB model can also reproduces the topological properties of the monolayer $Z_2Y\mathrm{CO}_2$, which is predicted as a second-order topological insulator [39]. The topological properties of our TB model can be directly diagnosed using the theory of topological quantum chemistry (TQC) [42, 45–47]. As shown in Fig. 3, the irreducible representations of valence band at all the high-symmetry points are calculated as $\Gamma_1 \oplus \Gamma_2 + X_3 \oplus X_3 + M_3 \oplus M_4$, which are induced by the $d_{x^2-y^2}$ and d_{z^2} orbital located at $1b$ Wyckoff position [see Fig. 4(b)]. However, in the four-band TB model, the $1b$ Wyckoff position is empty. This indicates that the four-band TB model established here must be nontrivial. According to the classification of higher-order topology [42, 48], it is a second-order topological insulator (SOTI).

A characteristic of the SOTI is the presence of corner states at specific corners of SOTI nanodisk. Here, based on the TB model, we calculate the spectrum for a nanodisk with 15×15 unit cells whose edges are on 110 and $1\bar{1}0$ directions. The results are plotted in Fig. 4(c-d), where four degenerate corner states in the gap of bulk state can be clearly observed. The degeneracy of these four corner states is protected by the S_{4z} symmetry of system. Similar to the low-energy bands in bulk,

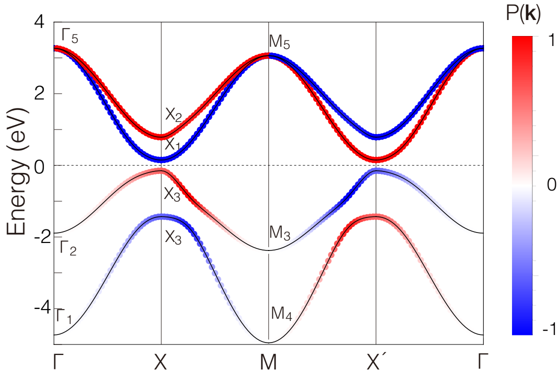

FIG. 3. Layer polarization $P(\boldsymbol{k})$ of TB bands obtained from Hamiltonian (3). The representation of the valence bands at high-symmetry points are labeled.

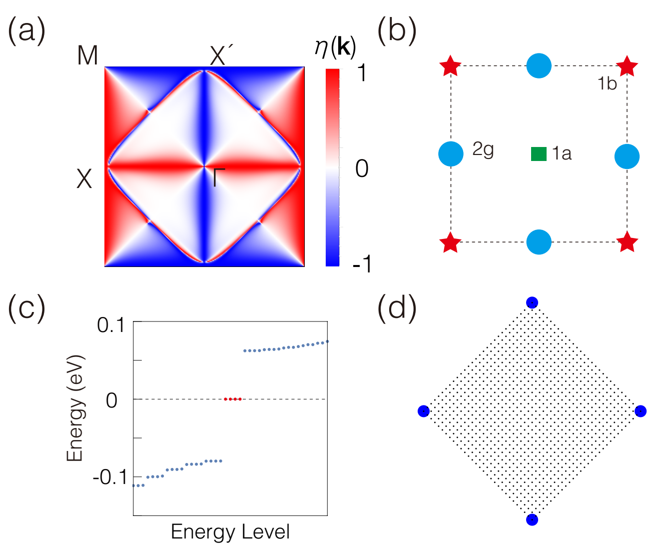

FIG. 4. (a) $\eta(\boldsymbol{k})$ of the TB model (3) in BZ. (b) Three Wyckoff positions of the monolayer Z_2YCO_2 in real space. In the TB model (3), the $2g$ position is occupied by atoms, while $1a$ and $1b$ positions are empty. (c) Spectra of the Z_2YCO_2 nanodisk, where four corner states (red dots) appear in the band gap. (d) The distribution of the corner states in real space.

the four corner states also have strong layer polarization. Again, due to the S_{4z} symmetry, the layer polarization of the corner states at x and y axis are opposite, consistent with the previous work [39].

IV. PHASE TRANSITIONS

In addition to reproducing the low-energy physics of monolayer Z_2YCO_2, the four-band TB model is itself physically interesting, and can host many topological phases under external fields. One can expect that these topological phases may be realized in the monolayer Z_2YCO_2 under suitable conditions.

TABLE IV. Fitted parameter α [in Eq. (6)]. α is in the unit of Å.

	TiSiCO	TiGeCO	ZrSiCO	ZrGeCO	HfSiCO	HfGeCO
α	-0.204	-0.182	-0.237	-0.241	-0.267	-0.249

Owing to the strong VLC effect, the most convenient way to control the bands of the TB model is applying a gate electric field normal to the plane of system, as it can produce an opposite electrostatic potential for the top and bottom atoms. Approximately, the effect of gate electric field can be incorporated in the TB model (3) by introducing the an on-site energy term,

$$\mathcal{H}_E = \alpha E \begin{pmatrix} 1 & 0 & 0 & 0 \\ 0 & 1 & 0 & 0 \\ 0 & 0 & -1 & 0 \\ 0 & 0 & 0 & -1 \end{pmatrix}, \tag{6}$$

where E is the electric field and α is a real parameter depending on the material details, like the separation of the top and bottom Z atoms, layer polarization of valley states, and the screening effect. The values of α for different monolayer Z_2YCO_2 are listed in Table IV, which is extracted from the first-principle calculations [see Appendix B]. When E is finite, both S_{4z} and $C_{2,110}$ symmetries of the system are broken, rendering the two valleys X and X' non-equivalent. As E increases (assuming $E > 0$), the band gap in X valley decreases while that in X' valley becomes lager. At a critical value $E = E_c$, the conduction and valence bands touch at X valley, forming a semi-Dirac point [49–51]. Interestingly, the semi-Dirac point exhibits a linear dispersion along k_x direction but a quadratic dispersion along k_y direction [see Fig. 5(a)], and can be considered as a critical point where two conventional Dirac points merge together. With the continuous increase of the gate field, the semi-Dirac point splits into two conventional Dirac points located at M-X path, as illustrated in Fig. 5(c). Since both Dirac points reside around X valley, we term this phase as valley-polarized topological Dirac semimetal (V-DSM).

The four-band TB model can also be tuned by symmetry-preserving perturbations like biaxial strain, which changes the value of the parameters in the original Hamiltonian (3). Consider a symmetry-preserving perturbation

$$\mathcal{H}_\delta = \delta(\cos k_x - \cos k_y) \begin{pmatrix} 1 & 0 & 0 & 0 \\ 0 & 1 & 0 & 0 \\ 0 & 0 & -1 & 0 \\ 0 & 0 & 0 & -1 \end{pmatrix}, \tag{7}$$

corresponding to the situation that the parameter $t_{i,\alpha}$

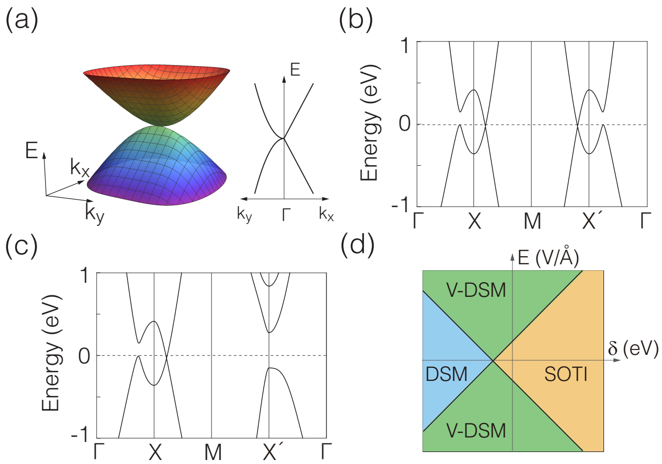

FIG. 5. (a) On the left, a 2D band structure illustrating a semi-Dirac point, and on the right, the dispersion of the semi-Dirac point's energy bands along high-symmetry paths. (b) and (c) are typical bands of Z_2YCO_2 in DSM and VPTDSM phase. (d) phase diagram of Z_2YCO_2 under gate electric field and symmetry-preserving perturbation. (b)(c)(d) are obtained using TB model of TiSiCO

($i = 1, 2$ and $\alpha = x, y$) by δ has been changed, while the other parameters unchange.

This perturbation changes the band gap at both valleys. Particularly, the band gap of system decreases when $\delta < 0$, and closes at a critical value $\delta = \delta_c$, in such case, there exist two semi-Dirac points residing at X and X' valleys, respectively. When $\delta < \delta_c$, the two semi-Dirac points become four symmetry-connected conventional Dirac points, and the system becomes a topological Dirac semimetal (DSM), as shown in Fig. 5(b). The phase diagram of the TB model under these two perturbations E and δ is plotted in Fig. 5(d).

V. CONCLUSION

In this work, we construct a four-band TB model for the TiSiCO-family monolayers (Z_2YCO_2) based on the d-orbitals of the two Z atoms. Via the theory of band representation, we show this four-band model is the minimal one that can capture the low-energy physics of the TiSiCO-family monolayers. Our TB model includes both inter-layer and intra-layer NN hoppings, and the hopping parameters are fitted to first-principle calculations by gradient descent method. Consequently, our model accurately reproduces the energy dispersion and the layer polarization of the bands around X and X′ valleys. Our model can also describe the valley-contrasted linear dichroism of the monolayer Z_2YCO_2. Furthermore, we demonstrate that the TB model is a SOTI, and exhibits topological corner states in its nanodisk. These results are consist with that calculated from first-principle calculations.

We then investigate the possible phase transitions of the TB model under different perturbations. Under a gate field and biaxial strain, the TB model is transformed from a SOTI to two distinct phases: valley-polarized topological Dirac semimetal and conventional topological Dirac semimetal. Therefore, our TB model not only effectively describes the low-energy properties of monolayer Z_2YCO_2, which greatly simplify the further study on monolayer Z_2YCO_2 materials, but also can be used to study the interplay between valley physics and higher-order topology.

Experimentally, one can use the molecular beam epitaxy technology to directly synthesize the monolayers. Besides, the previous work [52] studies the synthesis of quaternary compounds from the (IV-B, IV-A, IV-A, VI-A) groups and demonstrates that demonstrated that $ZrGe_xSi_{1-x}Te$ with x ranging from 0% to 100% can be experimentally synthesized. This indicates that the syntheses of bulk of TiSiCO-family materials is experimentally possible. Then, one can obtain the monolayer TiSiCO-family material from their bulk through mechanical exfoliation. The optical properties of the monolayers can be experimentally detected by linearly polarized photoluminescence measurements, and the gate-field induced phase transitions can be measured by the ordinary transport experiments as unusual field-dependent resistance.

ACKNOWLEDGMENTS

The authors thank J. Xun for helpful discussions. This work was supported by the NSF of China (Grants No. 12004035), and the National Natural Science Fund for Excellent Young Scientists Fund Program (Overseas). We gratefully acknowledge HZWTECH for providing computation facilities

Appendix A: Band analysis of the TiSiCO-family monolayers

Here, we study the band structure and their projection onto atomic orbitals of the monolayer Z_2YCO_2. The electronic band structures of the monolayers Z_2YCO_2 are calculated via the Vienna ab initio simulation package (VASP) [53, 54] and the Nanodcal package [58]. We have adopted the hybrid functional approach (HSE06) [55, 56] and the generalized gradient approximation with the Perdew-Burke-Ernzerhof (PBE) [57] to calculate the bands, and the results are shown in Fig. 6 and Fig. 7, respectively. The 2D Brillouin zone (BZ) was sampled using Monkhorst-Pack k-mesh with a size of 11×11×1. The energy cutoff was set to 550 eV and the energy convergence criteria was 10^{-6} eV.

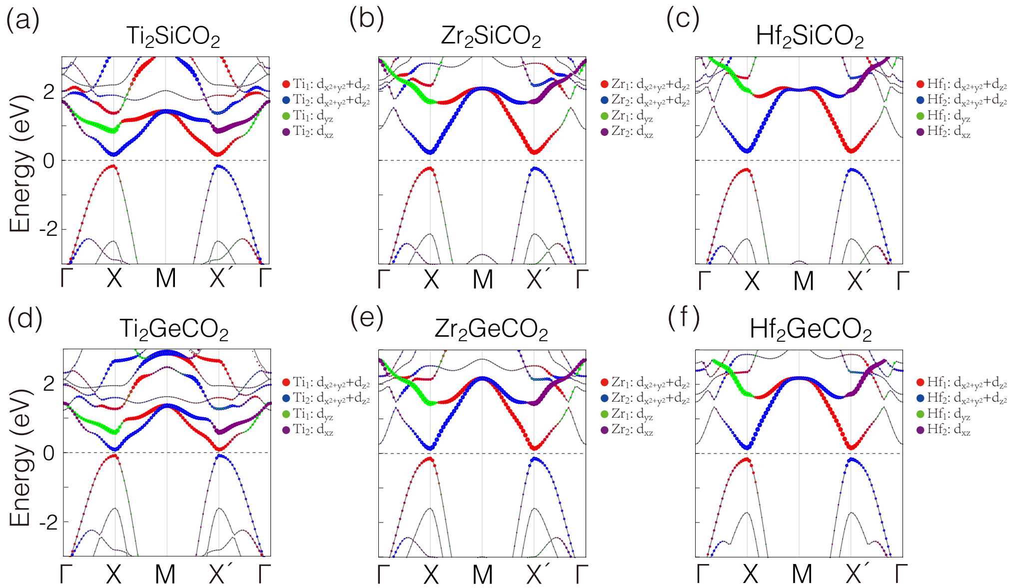

FIG. 6. HSE06 band structure of monolayer Z_2YCO_2 (Z = Ti, Zr, Hf; Y = Si, Ge) without SOC. The size of the colored circles is proportional to the weight of projection onto atomic orbitals.

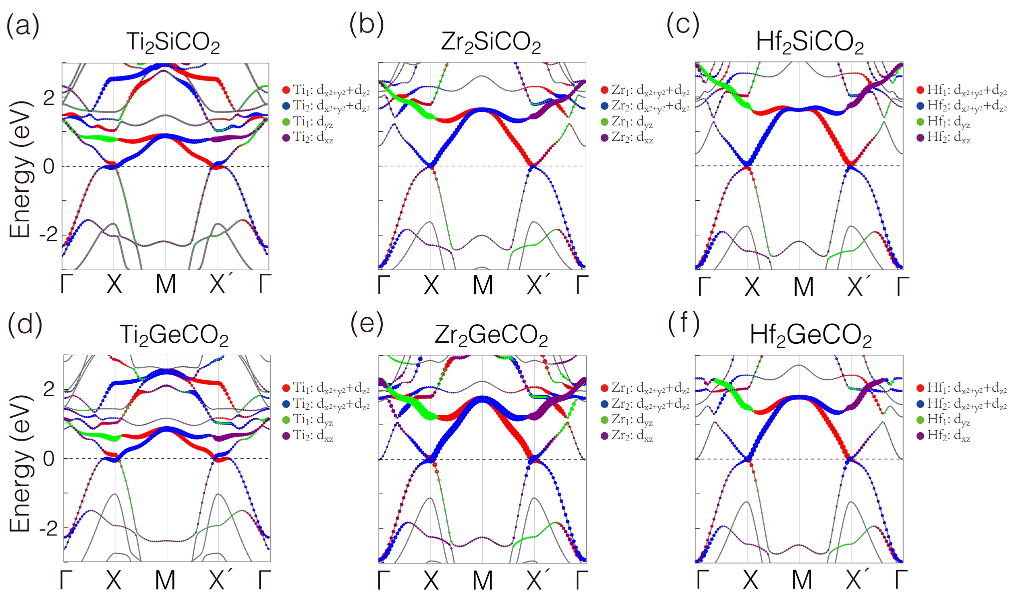

FIG. 7. PBE band structure of monolayer Z_2YCO_2 (Z = Ti, Zr, Hf; Y = Si, Ge) without SOC. The size of the colored circles is proportional to the weight of projection onto atomic orbitals.

Appendix B: Schematic illustration of the hopping in Hamiltonian (3)

To make the TB model (3) easier to understand, we plot a schematic illustration of the hopping in it, as shown in Fig. 8.

Appendix C: Gate field control of valley states in TiSiCO-family monolayers

Due to VLC, a gate-field control of the valley polarization can be realized in the monolayer Z_2YCO_2. The electronic band of the monolayer Z_2YCO_2 under a gate field of 0.05 eV/Å are shown in Fig. 9, from which the coefficient α in Eq. (6) can be obtained.

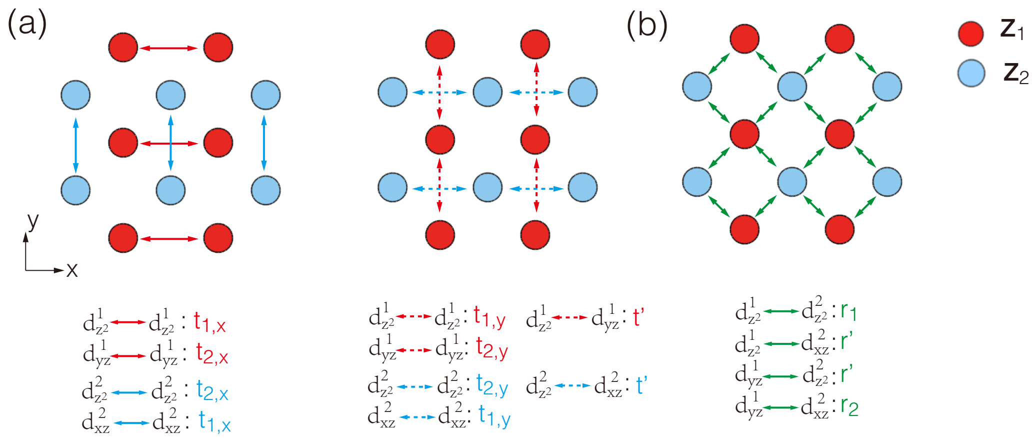

FIG. 8. Schematic diagram of the (a) intra-layer and (b) inter-layer hoppings in Hamiltonian (3), which are denoted by the double-headed arrows. Here, red and blue circles denote upper and lower Z atoms, respectively.

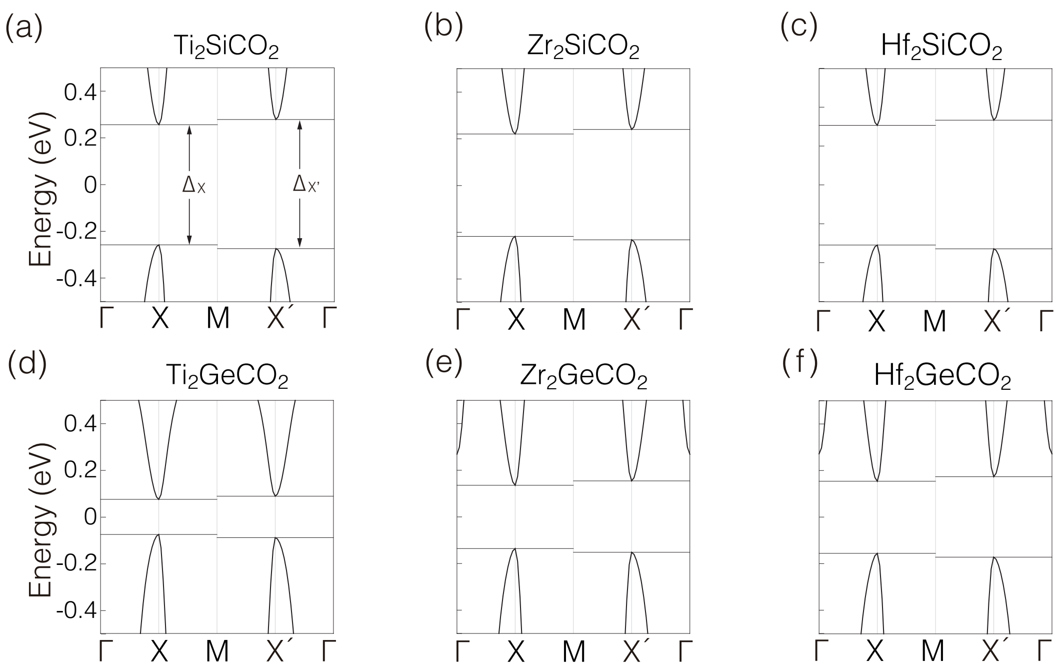

FIG. 9. (a-f) Electronic band structure of monolayer Z_2YCO_2 (Z = Ti, Zr, Hf; Y = Si, Ge) under a gate field of 0.05 eV/Å ,obtained from first-principle calculations. The gap at X and X' point is denoted as Δ_X and $\Delta_{X'}$. α is obtained by comparing the values of $\Delta_X - \Delta_{X'}$ from TB model (3) with Eq. (6) and that from first-principle calculations.

[1] A. Rycerz, J. Tworzydło, and C. W. J. Beenakker, Valley filter and valley valve in graphene, Nature Physics **3**, 172 (2007).

[2] O. Gunawan, Y. P. Shkolnikov, K. Vakili, T. Gokmen, E. P. De Poortere, and M. Shayegan, Valley susceptibility of an interacting two-dimensional electron system, Phys Rev Lett **97**, 186404 (2006).

[3] H. Yu, X. Cui, X. Xu, and W. Yao, Valley excitons in two-dimensional semiconductors, National Science Review **2**, 57 (2014).

[4] D. Xiao, W. Yao, and Q. Niu, Valley-contrasting physics in graphene: magnetic moment and topological transport, Phys Rev Lett **99**, 236809 (2007).

[5] D. Xiao, G. B. Liu, W. Feng, X. Xu, and W. Yao, Coupled spin and valley physics in monolayers of mos2 and other group-vi dichalcogenides, Phys Rev Lett **108**, 196802 (2012).

[6] W. Yao, D. Xiao, and Q. Niu, Valley-dependent optoelectronics from inversion symmetry breaking, Physical Review B **77**, 10.1103/PhysRevB.77.235406 (2008).

[7] T. Cai, S. A. Yang, X. Li, F. Zhang, J. Shi, W. Yao, and Q. Niu, Magnetic control of the valley degree of freedom of massive dirac fermions with application to transition metal dichalcogenides, Phys. Rev. B **88**, 115140 (2013).

[8] H. Pan, X. Li, H. Jiang, Y. Yao, and S. A. Yang, Valley-polarized quantum anomalous hall phase and disorder-induced valley-filtered chiral edge channels, Physical Review B **91**, 10.1103/PhysRevB.91.045404 (2015).

[9] J. R. Schaibley, H. Yu, G. Clark, P. Rivera, J. S. Ross, K. L. Seyler, W. Yao, and X. Xu, Valleytronics in 2d materials, Nature Reviews Materials **1**, 10.1038/natrevmats.2016.55 (2016).

[10] S. A. Vitale, D. Nezich, J. O. Varghese, P. Kim, N. Gedik, P. Jarillo-Herrero, D. Xiao, and M. Rothschild, Valleytronics: Opportunities, challenges, and paths forward, Small **14**, e1801483 (2018).

[11] Z. Zhu, A. Collaudin, B. Fauqué, W. Kang, and K. Behnia, Field-induced polarization of dirac valleys in bismuth, Nature Physics **8**, 89 (2011).

[12] G. Aivazian, Z. Gong, A. M. Jones, R.-L. Chu, J. Yan, D. G. Mandrus, C. Zhang, D. Cobden, W. Yao, and X. Xu, Magnetic control of valley pseudospin in monolayer wse2, Nature Physics **11**, 148 (2015).

[13] A. Srivastava, M. Sidler, A. V. Allain, D. S. Lembke, A. Kis, and A. Imamoğlu, Valley zeeman effect in elementary optical excitations of monolayer wse2, Nature Physics **11**, 141 (2015).

[14] X. Xu, W. Yao, D. Xiao, and T. F. Heinz, Spin and pseudospins in layered transition metal dichalcogenides, Nature Physics **10**, 343 (2014).

[15] D. Gunlycke and C. T. White, Graphene valley filter using a line defect, Phys. Rev. Lett. **106**, 136806 (2011).

[16] H. Pan, X. Li, F. Zhang, and S. A. Yang, Perfect valley filter in a topological domain wall, Phys. Rev. B **92**, 041404 (2015).

[17] H. Pan, X. Li, H. Jiang, Y. Yao, and S. A. Yang, Valley-polarized quantum anomalous hall phase and disorder-induced valley-filtered chiral edge channels, Phys. Rev. B **91**, 045404 (2015).

[18] Y. Jiang, T. Low, K. Chang, M. I. Katsnelson, and F. Guinea, Generation of pure bulk valley current in graphene, Phys. Rev. Lett. **110**, 046601 (2013).

[19] M. M. Grujić, M. i. c. v. Tadić, and F. m. c. M. Peeters, Spin-valley filtering in strained graphene structures with artificially induced carrier mass and spin-orbit coupling, Phys. Rev. Lett. **113**, 046601 (2014).

[20] L. Ju, Z. Shi, N. Nair, Y. Lv, C. Jin, J. Velasco, C. Ojeda-Aristizabal, H. A. Bechtel, M. C. Martin, A. Zettl, J. Analytis, and F. Wang, Topological valley transport at bilayer graphene domain walls, Nature **520**, 650 (2015).

[21] M. Sui, G. Chen, L. Ma, W.-Y. Shan, D. Tian, K. Watanabe, T. Taniguchi, X. Jin, W. Yao, D. Xiao, and Y. Zhang, Gate-tunable topological valley transport in bilayer graphene, Nature Physics **11**, 1027 (2015).

[22] W.-Y. Tong, S.-J. Gong, X. Wan, and C.-G. Duan, Concepts of ferrovalley material and anomalous valley hall effect, Nature Communications **7**, 13612 (2016).

[23] V. H. Nguyen, S. Dechamps, P. Dollfus, and J.-C. Charlier, Valley filtering and electronic optics using polycrystalline graphene, Phys. Rev. Lett. **117**, 247702 (2016).

[24] A. R. Akhmerov, J. H. Bardarson, A. Rycerz, and C. W. J. Beenakker, Theory of the valley-valve effect in graphene nanoribbons, Phys. Rev. B **77**, 205416 (2008).

[25] A. Cresti, G. Grosso, and G. P. Parravicini, Valley-valve effect and even-odd chain parity in $p-n$ graphene junctions, Phys. Rev. B **77**, 233402 (2008).

[26] P. San-Jose, E. Prada, E. McCann, and H. Schomerus, Pseudospin valve in bilayer graphene: Towards graphene-based pseudospintronics, Phys. Rev. Lett. **102**, 247204 (2009).

[27] Z. Qiao, J. Jung, Q. Niu, and A. H. MacDonald, Electronic highways in bilayer graphene, Nano Letters **11**, 3453 (2011).

[28] Z. Qiao, J. Jung, C. Lin, Y. Ren, A. H. MacDonald, and Q. Niu, Current partition at topological channel intersections, Phys. Rev. Lett. **112**, 206601 (2014).

[29] J. Li, R.-X. Zhang, Z. Yin, J. Zhang, K. Watanabe, T. Taniguchi, C. Liu, and J. Zhu, A valley valve and electron beam splitter, Science **362**, 1149 (2018).

[30] J. L. Garcia-Pomar, A. Cortijo, and M. Nieto-Vesperinas, Fully valley-polarized electron beams in graphene, Phys. Rev. Lett. **100**, 236801 (2008).

[31] M. Settnes, S. R. Power, M. Brandbyge, and A.-P. Jauho, Graphene nanobubbles as valley filters and beam splitters, Phys. Rev. Lett. **117**, 276801 (2016).

[32] S.-g. Cheng, H. Liu, H. Jiang, Q.-F. Sun, and X. C. Xie, Manipulation and characterization of the valley-polarized topological kink states in graphene-based interferometers, Phys. Rev. Lett. **121**, 156801 (2018).

[33] Z. M. Yu, S. Guan, X. L. Sheng, W. Gao, and S. A. Yang, Valley-layer coupling: A new design principle for valleytronics, Phys Rev Lett **124**, 037701 (2020).

[34] F. Zhang, J. Jung, G. A. Fiete, Q. Niu, and A. H. MacDonald, Spontaneous quantum hall states in chirally stacked few-layer graphene systems, Phys. Rev. Lett. **106**, 156801 (2011).

[35] W. Yao, S. A. Yang, and Q. Niu, Edge states in graphene: From gapped flat-band to gapless chiral modes, Phys. Rev. Lett. **102**, 096801 (2009).

[36] G.-B. Liu, W.-Y. Shan, Y. Yao, W. Yao, and D. Xiao, Three-band tight-binding model for monolayers of group-vib transition metal dichalcogenides, Physical Review B **88**, 10.1103/PhysRevB.88.085433 (2013).

[37] G. B. Liu, D. Xiao, Y. Yao, X. Xu, and W. Yao, Electronic structures and theoretical modelling of two-dimensional group-vib transition metal dichalcogenides, Chem Soc Rev **44**, 2643 (2015).

[38] N. M. R. Peres, Colloquium: The transport properties of graphene: An introduction, Rev. Mod. Phys. **82**, 2673 (2010).

[39] Y. Han, C. Cui, X.-P. Li, T.-T. Zhang, Z. Zhang, Z.-M. Yu, and Y. Yao, Cornertronics in two-dimensional second-order topological insulators (2023), arXiv:2306.08384 [cond-mat.mes-hall].

[40] Bilbao crystallographic server: www.cryst.ehu.es.

[41] G.-B. Liu, Z. Zhang, Z.-M. Yu, and Y. Yao, Msgcorep: A package for corepresentations of magnetic space groups, Computer Physics Communications **288**, 108722 (2023).

[42] B. Bradlyn, L. Elcoro, J. Cano, M. G. Vergniory, Z. Wang, C. Felser, M. I. Aroyo, and B. A. Bernevig, Topological quantum chemistry, Nature **547**, 298 (2017).

[43] C. Lemaréchal, Cauchy and the gradient method, Doc Math Extra **251**, 10 (2012).

[44] T. Cao, G. Wang, W. Han, H. Ye, C. Zhu, J. Shi, Q. Niu, P. Tan, E. Wang, B. Liu, and J. Feng, Valley-selective circular dichroism of monolayer molybdenum disulphide, Nat Commun **3**, 887 (2012).

[45] J. Kruthoff, J. de Boer, J. van Wezel, C. L. Kane, and R.-J. Slager, Topological classification of crystalline insulators through band structure combinatorics, Phys. Rev. X **7**, 041069 (2017).

[46] H. C. Po, A. Vishwanath, and H. Watanabe, Symmetry-based indicators of band topology in the 230 space groups, Nature Communications **8**, 50 (2017).

[47] Z.-D. Song, L. Elcoro, and B. A. Bernevig, Twisted bulk-boundary correspondence of fragile topology, Science **367**, 794 (2020).

[48] F. Schindler, A. M. Cook, M. G. Vergniory, Z. Wang, S. S. P. Parkin, B. A. Bernevig, and T. Neupert, Higher-order topological insulators, Science Advances **4**, eaat0346 (2018).

[49] V. Pardo and W. E. Pickett, Half-metallic semi-dirac-point generated by quantum confinement in tio_2/vo_2 nanostructures, Phys. Rev. Lett. **102**, 166803 (2009).

[50] A. M. Cook, M. F. B, F. de Juan, S. Coh, and J. E. Moore, Design principles for shift current photovoltaics, Nat Commun **8**, 14176 (2017).

[51] P. Sinha, S. Murakami, and S. Basu, Landau levels and magneto-optical transport properties of a semi-dirac system, Phys. Rev. B **105**, 205407 (2022).

[52] Chwanchin, Wang, Timothy, and Hughbanks, Main group element size and substitution effects on the structural dimensionality of zirconium tellurides of the zrsis type, Inorganic Chemistry **34**, 5524–5529 (1995).

[53] G. Kresse and J. Furthmüller, Efficient iterative schemes for ab initio total-energy calculations using a plane-wave basis set, Physical Review B **54**, 11169 (1996).

[54] G. Kresse and J. Furthmüller, Efficiency of ab-initio total energy calculations for metals and semiconductors using a plane-wave basis set, Computational Materials Science **6**, 15 (1996).

[55] J. Heyd, G. E. Scuseria, and M. Ernzerhof, Hybrid functionals based on a screened Coulomb potential, The Journal of Chemical Physics **118**, 8207 (2003).

[56] A. V. Krukau, O. A. Vydrov, A. F. Izmaylov, and G. E. Scuseria, Influence of the exchange screening parameter on the performance of screened hybrid functionals, The Journal of Chemical Physics **125**, 224106 (2006).

[57] J. P. Perdew, K. Burke, and M. Ernzerhof, Perdew, Burke, and Ernzerhof Reply:, Physical Review Letters **80**, 891 (1998).

[58] J. Taylor, H. Guo, and J. Wang, Ab initio modeling of quantum transport properties of molecular electronic devices, Phys. Rev. B **63**, 245407 (2001).